

New insights on the central stellar population and gas outflow in NGC 1068 from YJH spectroscopy with SPHERE/VLT

Pierre Vermot¹, Yann Clénet¹, and Damien Gratadour¹

LESIA, Observatoire de Paris, Université PSL, CNRS, Sorbonne Université, Univ. Paris Diderot, Sorbonne Paris Cité, 5 place Jules Janssen, 92195 Meudon, France

Submitted - Not yet accepted for publication

ABSTRACT

Aims : In this paper we aim at characterizing the properties of stars, dust and gas and their spatial distribution in the central region of the Seyfert 2 galaxy NGC1068.

Method : Our study is based on NIR (YJH, 0.95-1.650 μm , $R=350$) long slit spectroscopy observations of NGC 1068's central region with 0.4" spatial resolution. On the one hand we decomposed the observed continuum emission into three components: hot dust, stars and scattered light from the central engine to measure their contributions at various distances from the nucleus. On the other hand, we measured fluxes and doppler shifts for the emission lines present in our spectrum to probe the physical conditions of the Narrow Line Region.

Results : Dust and stars are the main contributors to the continuum, but scattered light from the central engine is also detected in the very central region. Together, those three components are well reproducing the observed continuum. The dust emission is well modeled by a 800K blackbody, is spatially unresolved and only located in the very central region. The stellar content is ubiquitous and harbours a 250 pc cusp centered around the nucleus, overimposed to a young stellar background. The spectrum of the cusp is consistent with a 120 Myr single stellar population. Finally, the emission lines exhibit a significant doppler shift, consistent with a radial outflow from the nucleus in a biconical structure. The $[Fe II]$ behaviour strongly differs from other lines, suggesting that it arises from a different structure.

Key words. Infrared: Galaxies; Galaxies: active, Seyfert, stellar content, individual: NGC 1068; Techniques: spectroscopic

1. Introduction

NGC 1068 is a spiral galaxy ((R)SA(rs)b) whose close location ($z=0.00379$, $D=16.25$ Mpc $\Leftrightarrow 79$ pc.arcsec⁻¹) and important luminosity (several $10^{11} L_{\odot}$ according to Pier et al. 1994) led to a wealth of observations that made it a key tool in the understanding of Active Galactic Nuclei (AGN). Indeed, NGC 1068 is the archetypal Seyfert 2 galaxy, harbouring a distinct Narrow Line Region (NLR) (Macchetto et al. 1994) and a strong dusty source of infrared radiation (Gratadour et al. 2006) hiding a Seyfert 1 nucleus (Antonucci & Miller 1985; Antonucci 1993). However, those observations revealed many different structures in the nuclear region, with complex interactions and spatial distributions, still letting unresolved questions on the physical processes taking place in AGN.

NGC 1068 harbours a supermassive black hole (SMBH) with a mass dynamically estimated to $8.6 \pm 0.5 \times 10^6 M_{\odot}$ (Kormendy et al. 2011) associated to an accretion disk, the main source of the luminosity in the commonly accepted description of AGN (Rees 1984; Hickox & Alexander 2018) and referred afterwards as central engine (CE). This central engine is hidden from the observer by an obscuring material, composed of gas and dust (Hickox & Alexander 2018) and often referred to as a *dusty torus*. This structure is known to be parsec-scale (Jaffe et al. 2004; Poncelet et al. 2006) and with temperatures at least ranging from 320 K (Jaffe et al. 2004) to 1200 K (Gratadour et al. 2003). In radio wavelengths, two radio jets extending up to several hundred parsecs from the SMBH are observed (Wilson & Ulvestad 1983). These jets seem to interact with the close

environment of the nucleus: they are surrounded by several clouds detected in mid-infrared (Bock et al. 2000) and the northern jet is deviated by at least one of them, located at 25 pc North from the center (Gallimore et al. 1996).

With a similar scale than the jets (several hundred pc) stands a conspicuous NLR, originally observed in the UV and optical wavelengths (Macchetto et al. 1994; Kraemer & Crenshaw 2000; Cecil et al. 2002) and furtherly observed in the near-infrared (Davies et al. 2007b; Martins et al. 2010b; Exposito et al. 2011; Riffel et al. 2014). These observations revealed that the NLR harbours a bicone shape oriented NE-SW with evidences of motion of the gas: the northern part is blueshifted and the southern one redshifted, interpreted as a radial outflow from the nucleus with an inclined bicone structure (Das et al. 2006). Two main ionization mechanisms for the NLR are invoked to explain the behavior of the observed emission lines: photoionization from the CE (Kraemer & Crenshaw 2000; Hashimoto et al. 2011) and ionization from shocks due to the interaction with the jet (Dopita & Sutherland 1996; Kraemer & Crenshaw 2000; Exposito et al. 2011). Stars have also been mentioned as a possible source of ionisation (Nazarova 1996; Exposito et al. 2011).

As observed by Origlia et al. (1993) and confirmed by further studies, stars are undoubtedly present around NGC 1068's nucleus. Stellar population synthesis (Martins et al. 2010a) and emission line ratios diagnostics (Origlia et al. 1993) both indicate relatively recent star formation around the nucleus.

Even if the presence of those four components (CE, dust, NLR and stars) in NGC 1068's nucleus is well established, many open

questions remain: how are they spatially distributed? What is their relative contribution to flux at different wavelengths? What are the physical conditions in this region (dust temperature, gas kinematics, ionisation mechanisms)? How old is the stellar population?

In this paper, we investigate these questions using SPHERE/VLT, and in particular its long-slit spectroscopy mode. This instrument gives us access to a spectral region of great interest for such a study (YJH, $0.95 - 1.65 \mu\text{m}$). First, it is an intermediate spectral domain, where the thermal emission from hot dust, the stars and the central engine can contribute to the continuum, making it possible to study the three simultaneously. Secondly it contains many emission lines, allowing us to probe the gas physical conditions and its excitation mechanisms. Finally the extinction by dust, even if still present at those wavelengths, is much lower than in the optical, giving us the possibility to probe for deeper regions.

The paper is organised as follows : in Sect. 2 we describe the observations and the data reduction. Section 3 presents our analyses of the continuum emission and spectral features, that are then discussed in Sect. 4. Section 5 is dedicated to a brief summary and conclusions.

2. Observation and data reduction

2.1. Observations

SPHERE (Beuzit et al. 2008) is an extreme adaptive optics (AO) system and coronagraphic facility installed at the UT3 Nasmyth focus of the VLT, primarily designed for exoplanet characterization. Observations were obtained in the night of December 5, 2014, during the science verification program. We used the IRDIS subsystem in its long slit spectroscopy mode (LSS, Vigan et al. 2008) with medium resolution (MRS), covering the range $0.95 - 1.65 \mu\text{m}$ with $R \sim 350$. We used a classical Lyot coronagraph with $0.2''$ radius, first positioned on the bright core source to avoid contamination of the surrounding region (dataset named SPH1), then with a slight offset in order to observe this bright core (SPH2). In both cases the spatial scale is $12.25 \text{ mas.pixel}^{-1}$, the linear dispersion is $1.13 \text{ nm.pixel}^{-1}$ (measured from the calibration lamp emission lines) and the slit ($11'' \times 0.09''$) was crossing the photocenter with $PA = 12^\circ$.

The sky emission was measured outside the galaxy, $144''$ south-east to the nucleus. These observations were followed by the observation of BD+00413, a close G0 calibration star with accurate 2MASS photometry in the H band, $H = 9.591 \pm 0.026$ (Cutri et al. 2003). The airmass went from 1.1 at the beginning of the run to 1.2 at the end. The seeing was not good (from $1.2''$ to $1.5''$ according to the observation log) leading to a poor AO correction and a final spatial resolution of $0.35''$ in the H band (FWHM measured on the central source, which is known to be unresolved with SPHERE in the H band Gratadour et al. (2015). Integration time and number of exposures are presented in Table 1 for each dataset.

Table 1. Observation summary

Observation's name	Number of exposures	Duration of 1 exposure (s)	Integration time (s)
SPH1	21	64	1344
SPH2	15	64	960
SKY	9	64	576
BD+00413	3	64	192

2.2. Data reduction

We divided the spectral images by the instrument's flat-field response, obtained with a per-pixel linear fit on lamp flat-field acquisitions with different integration times. A bad-pixel map was created by selecting pixels whose response or variability were outside a 3-sigma region around the associated mean on all pixels. Bad-pixel values were replaced by linearly interpolated values from surrounding pixels. We corrected the images from shear distortion using the correction matrix provided by the ESO's manual, and corrected from a second order spectral distortion measured on the calibration lamp spectrum. Each individual SPHERE image contains two spectral images associated to the two polarimetric channels. Since we did not use the polarimetric mode, both channels were isolated and treated as independant images. We finally performed the mean of all spectral images. We applied this method to the object, the calibration star and the sky images. Finally, we combined SPH1 and SPH2 by taking the mean of the overlapping regions (accounting a $0.4''$ spatial offset between the two observations) and performed sky subtraction.

We performed wavelength calibration with a linear fit on the positions of calibration lamp emission lines. Afterwards we measured atmospheric transmission by comparing the reference star's spectrum to the predicted spectrum of a G0 star (Pickles 1998), and corrected the object's spectra from it. We then performed flux calibration with the 2MASS H-magnitude of BD-00413.

We associate the uncertainty on each spectral image's pixel to the standard deviation of its values on the different frames before they are averaged. The flux calibration is an important contributor to our errors ($\sim 30\%$).

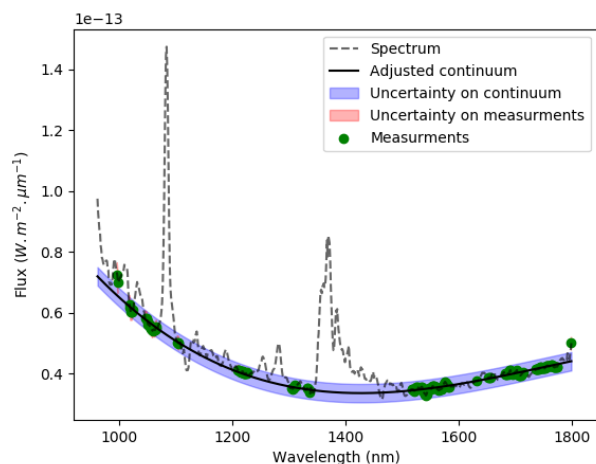


Fig. 1. Extraction of the continuum for the spectrum integrated on all the spatial dimension of the slit. The dashed line represents the observed spectrum, the green disks represent the sample values for continuum measurement and the solid line is the adjusted 4th degree polynome. Uncertainty on the adjusted continuum is displayed in blue.

3. Analysis

We constructed two synthetic spectral images, one containing only the continuum emission, the other one only the spectral features. To estimate the continuum emission we selected a few

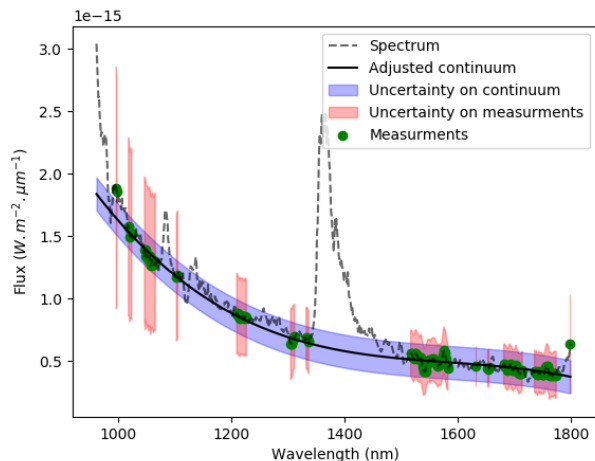


Fig. 2. Same as Fig. 1 but for a 0.3'' region 3'' North to the nucleus. Uncertainties on the sample values are displayed in red.

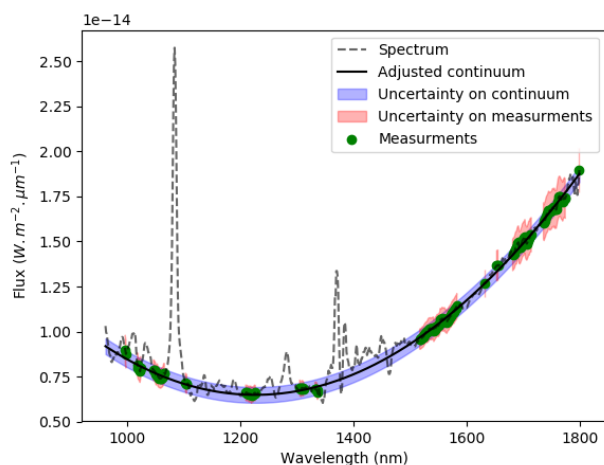


Fig. 3. Same as Fig. 1 but for the central 0.3'' region. Uncertainties on the sample values are displayed in red.

wavelengths free from emission or absorption features and fitted a 4th degree polynomial on those points at each position of the slit. This method provides us with a continuum spectral image that we subtract to the original one in order to only get the continuum-free contribution.

3.1. Continuum emission analysis

Examples of the continuum extraction for three regions are presented in Figs. 1, 2 and 3. Figure 1 presents the spectrum integrated on the entire spatial dimension, and the continuum extracted from it. It exhibits a "U" shape with a minimum located around 1400 nm. Figure 2 represents in the same way the spectrum integrated over a 0.3'' aperture, 3'' north to the nucleus, with the associated continuum emission. It shows an increase in the flux at short wavelengths. The southern spectrum is very similar. Finally, Fig. 3 is the integrated spectrum of the central region, with 0.3'' aperture, that emits strong emission toward long wavelength.

On the resulting continuum spectral image, we noticed the presence of a significant uniform background. Its contribution

has been measured by taking the mean continuum on a 0.5'' aperture at the extreme South of the slit (identical to the background measured at the extreme North of the slit) and has been subtracted to the whole spectrum. We briefly discuss the nature of this continuum at the end of this section. Otherwise, the continuum will be considered background subtracted.

Figure 4 represents the profiles of the continuum emission along the slit at 1000 nm and 1750 nm. The black profile (1750 nm), representing the component peaking at long wavelengths, is unresolved with our spatial resolution. The blue one (1000 nm), representing the short-wavelength component, exhibits a much wider profile.

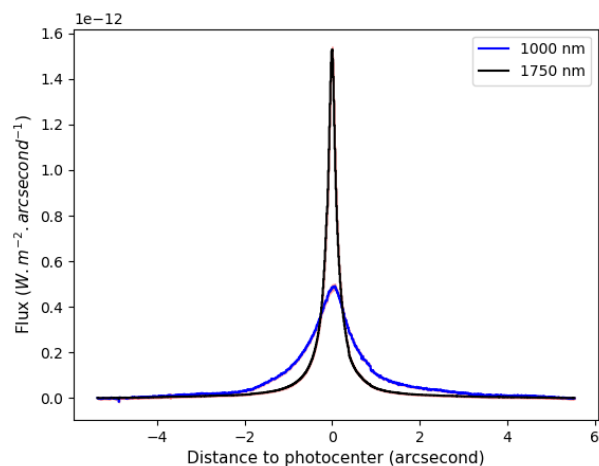


Fig. 4. Spatial profile of the continuum emission at short ($\lambda = 1000$ nm, blue curve) and long ($\lambda = 1750$ nm, black curve) wavelengths

The spectral behavior, the location and the spatial extent of those two main components give us strong indications regarding their nature. The component peaking at long wavelengths is very likely related to the obscuring material predicted by the unified model of AGN. The other component, the short-wavelength peaking one, is associated with stellar population. As mentioned before, studies also indicate that light from the central engine may be a significant contributor to the continuum (Crenshaw & Kraemer 2000; Martins et al. 2010b), hence we will try to identify it as well.

In this part, we aim at disentangling the spatial contributions from the stars, the hot dust and the central engine in the observed NIR continuum emission. For this purpose we simulated spectra for those 3 components and adjusted their relative contributions to the measured continuum.

To represent the stellar component, we chose a single stellar population (SSP) evolutionary model provided by GALEV (Kotulla et al. 2009) with a Salpeter IMF. We then extracted spectra for ages ranging from very young ($t = 8$ Myr) to intermediate ($t = 400$ Myr) stellar populations (intermediate age cannot be distinguished from older population in our spectral range). Considering that the circumnuclear region (defined hereafter as the region located further than 1'' from the photocenter) is mainly composed of stars, we used the continuum measured in this region to test our populations and observed that the 120

Myr one provides the best fit to our data.

Dust is supposed to be present at temperatures ranging from 320 K (Jaffe et al. 2004) to sublimation at $T \sim 1400$ K (Mor & Netzer 2012). However, our spectral range is poorly sensitive to temperatures below 700 K and dust at high temperature is expected to be located at the very center of the obscuring structure and so to be hidden from the observer by the latter. Hence, we modeled the dust emission contribution by a blackbody component at 800 K, which is consistent with temperature estimates from Martins et al. (2010b), and provides good fits to our data (example : Fig. 5).

The central engine component can be modeled by a power-law $F_\lambda = \lambda^{-\alpha}$ typically with $0 < \alpha < 1.5$. According to the AGN unified model, a good estimation for the spectral shape of the central engine can be obtained by looking at Seyfert 1 spectra. In their AGN atlas, Riffel et al. (2006) observed that the Sy1's NIR spectra can be well described by a broken power-law with a steep continuum below 1100 nm and an almost flat continuum redwards. We make the assumption that the blue steep continuum arises from stars, and thus that the central region contribution is mainly flat, so from now on we will use $\alpha = 0$ to represent the central engine. We notice that larger values of α do not change significantly our result, the slope of the associated spectrum staying well below the one from the stellar component anyway.

The continuum spectrum can be very well decomposed into those three components (800 K blackbody, 120 Myr single stellar population and λ^{-0} emission). Figure 5 displays the decomposition of the continuum integrated on the 0.3" central region. We can observe that the three components are significantly present even if the hot dust largely dominates. Figure 6 represents the same decomposition for a spectrum integrated from 2" to 2.5" north of the CE. It confirms that this region is largely dominated by stars. For comparison purpose we also present the decomposition of the continuum integrated on all the spatial dimension of the slit in Fig. 7, revealing that the main contributor is stellar content, followed by hot dust. In the overall spectrum, the central engine contribution is low.

The above decomposition has been performed at every position of the slit (rebinned by a factor 12 to match half the 0.3" spatial resolution of our observation) and is presented in Fig. 8. This reveals an unresolved central component dominated by dust with a significant portion of light coming from the central nucleus. The stellar content is distributed in a cluster with FWHM $\sim 1.5''$ centered on the nucleus.

Continuum background analysis

As shown in Fig. 9 the components used to describe the central region fail to reproduce the observed background continuum. Changing the stellar population for a younger one can slightly improve the quality of the fit, but our best explanation (presented in Fig. 10) is that the background is largely dominated by very hot stars, with a little contribution from hot dust. Such stars in YJH can simply be modeled by a blackbody in a Rayleigh-Jeans regime (valid for $T > 12000$ K) and provide a good fit to our data. This important contribution from hot stars is surprising but consistent with the very important starburst activity detected in

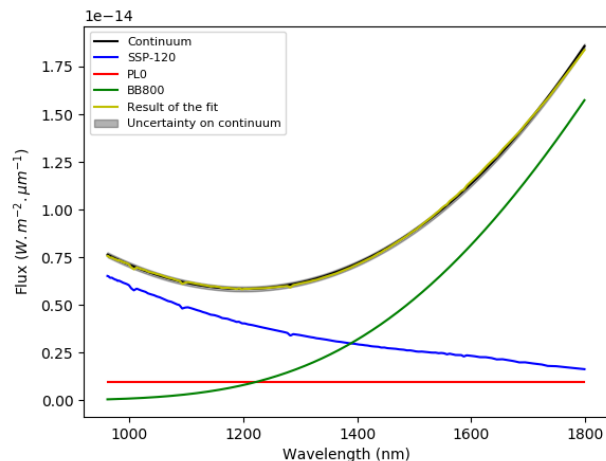


Fig. 5. Adjustment of the continuum in the central 0.3". The black line represents the measured continuum. The blue, green and red lines respectively represent the adjusted contribution of the 40 Myr Single Stellar Population, the 800 K blackbody and the flat continuum. The yellow line represents the sum of those contributions.

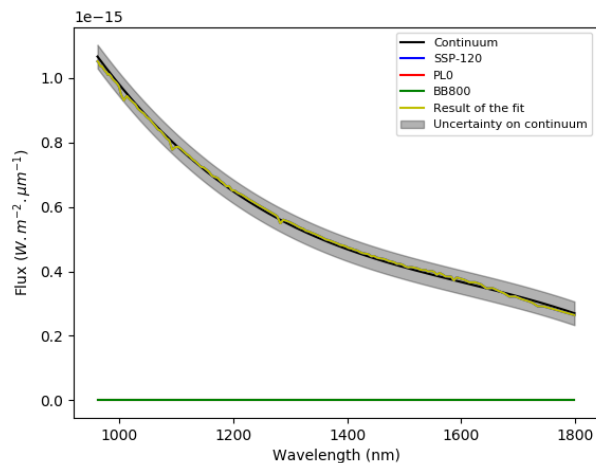


Fig. 6. Same as Fig. 5 but for a 1" aperture around the +2" North position.

NGC 1068 by previous studies (Romeo & Fathi 2016, and references therein).

3.2. Analysis of spectral features

This subsection describes the properties of the spectral features detected in the continuum free image, resulting from the decomposition described in the introduction of this section. At least 11 emission and 4 absorption features are detected.

The identification of the emission lines has been made following Martins et al. (2010b) and is presented in Table 2. Identification of the absorption features is discussed in Sect. 4.

Spatial distribution of the emission lines

In this part we present our measurements of the emission line flux distribution along the slit. For this purpose we used two methods to compute the emission line fluxes, the first one is

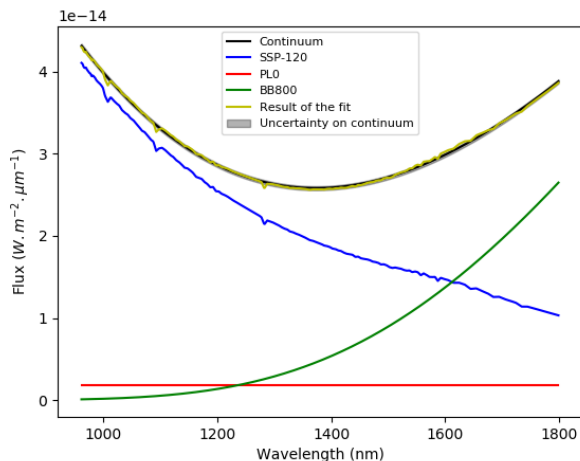


Fig. 7. Same as Fig. 5 but for the continuum integrated on all the spatial dimension of the slit.

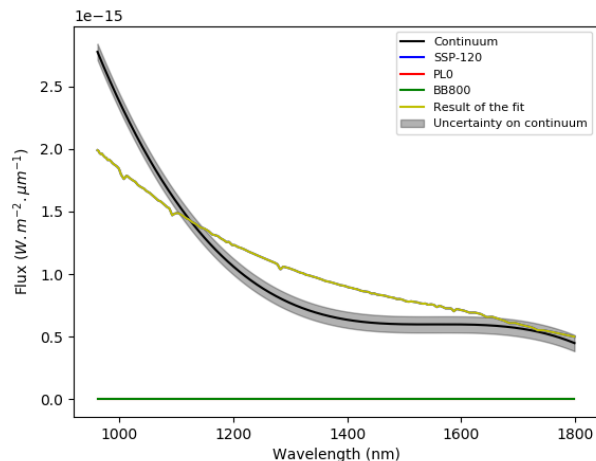


Fig. 9. Same as Fig. 5 but for the background continuum.

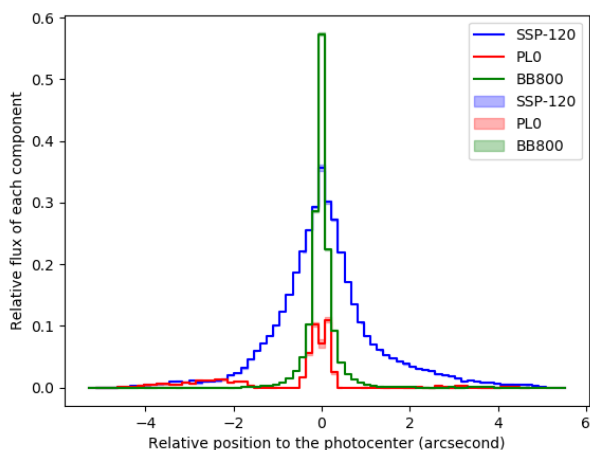


Fig. 8. Flux of each component relative to the photocenter's total flux. The blue, green and red lines represent the adjusted contribution of the 40 Myr Single Stellar Population, the 800 K blackbody and the flat continuum.

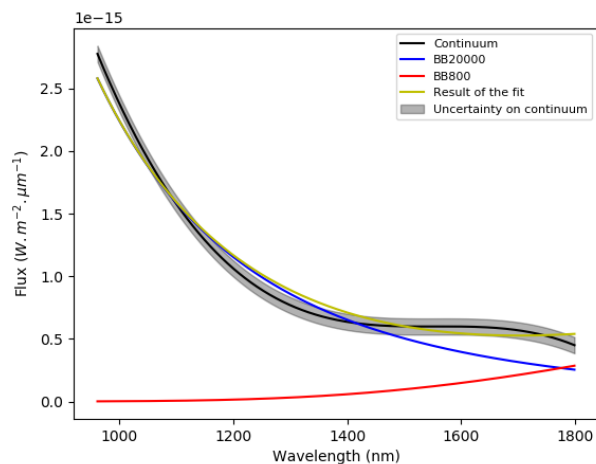


Fig. 10. Final adjustment of the background continuum. The black line represents the measured continuum. The blue and the red lines respectively represent the adjusted contributions of the 20000 K and 800 K blackbodies. The yellow line represents the sum of those contributions.

a direct sum of the pixel values along all the spectral range where flux is detected for the considered line. This method is robust and can be applied even in low SNR regions. Hence it was used for most of our lines. A double gaussian fit was used as a second method for the two couples of overlapping lines: He I - Pa γ and [S IX] - [Fe II] 1257. In order to improve the quality of our flux measurements for the [S IX] - [Fe II] 1257 overlapping lines, we set the central wavelengths of the lines as fixed parameters in our fit and impose an equal width to both lines. We extracted spatial profiles for 10 of our lines whose main characteristics (position of the maximum of emission and spatial extent) are presented in Table 2. We could not extract informations on [S VIII] because it is located in a region with poor SNR and may result from the contribution of different close lines, detected in Martins et al. (2010a). Considerations on the position of the maximum of emission and on the spatial extent brings out two categories of lines. The first category contains all the lines that have a maximum emission located near the photocenter and a spatial extent smaller than 4" (~ 350 pc). The majority of the lines falls in this category, with the exception

of the two [Fe II] lines, forming a second category whose maximum of emission are respectively located at 0.8" and 0.9" North and whose spatial extents are twice as large as those of the first category. Flux distribution for representative lines of each category are presented in Figs. 11 and 12 : He I for the first one and [Fe II] 1643 for the second one. Spatial distribution of other emission lines are available in Appendix A.

Doppler shift in emission lines

Using a gaussian fit on the emission lines with significant SNR, we have been able to measure shifts in their central wavelengths. These shifts are associated to a Doppler effect and will be discussed in speed units, rest speed being measured in the photocenter.

The two categories previously identified from considerations on spatial distribution are still relevant here: there are strong differences between the behavior of [Fe II] 1643 and other measur-

Table 2. Emission lines summary. The wavelengths are given in rest frame. The measure of the spatial extent is approximative and only given for qualitative comparisons.

Identification of the line	Wavelength (nm)	Maximum flux position (")	Spatial extent (")
[S VIII]	991	/	/
He II	1012	0.15	4.0
[S II]	1032	0.3	3.5
He I	1083	0.0	4.0
Pa γ	1093	0.0	4.0
[P II]	1188	0.0	3.5
[S IX]	1252	0.0	3.0
[Fe II]	1257	0.9	8.0
Pa β	1272	0.0	4.0
[Si X]	1430	0.2	2.5
[Fe II]	1643	0.8	7.0

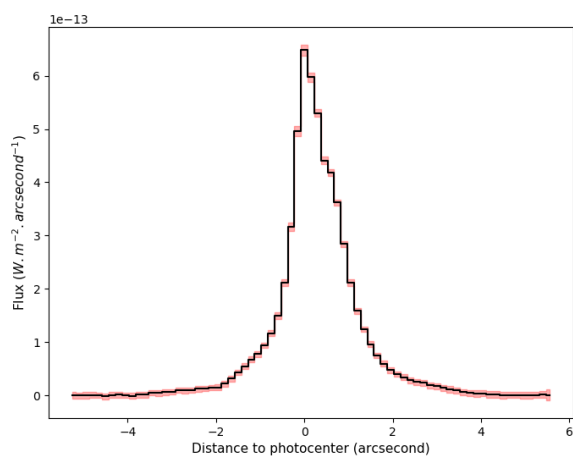


Fig. 11. Flux of He I as a function of the position on the slit, with 0.15" bins. The red region represents 3-sigma uncertainties.

able lines (no velocity shift can be measured for [Fe II] 1257 due to its overlapping with [S IX]). We present the results for He I and [Fe II] 1643 in Figs. 13 and 14, still considering that He I is representative of the others emission lines. Velocity plots for other lines are presented in appendix B when available. The two velocity profiles are very different, both in shape and amplitude.

Starting from the center, He I exhibits an increase in speed in both directions, blueshifted in the North and redshifted in the South, until reaching a maximum just before 2" ($\sim 150 pc$) where it quickly slows down to the rest speed. With respect to the CE location, the shift goes up to $140 \pm 10 km.s^{-1}$ in the northern region and up to $210 \pm 25 km.s^{-1}$ in the south. [Fe II] 1643 on the other hand exhibits redshift in both directions, a strong one in the northern region ($600 \pm 100 km.s^{-1}$) and a slighter one in the south ($100 \pm 50 km.s^{-1}$).

Spatial profiles of absorption lines equivalent width

Two couples of absorption features are weakly but surely detected in our spectrum. The first one contains lines at 1111 nm and 1118 nm and the second one at 1590 nm and 1620 nm. For each couple we present the spatial distribution of equivalent

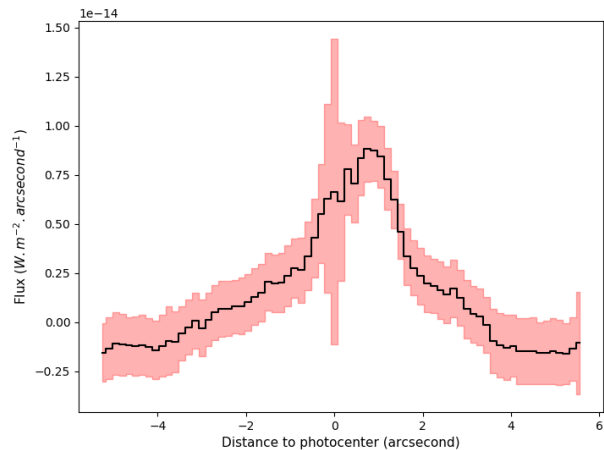


Fig. 12. Flux of [Fe II] $\lambda 1643$ as a function of the position on the slit, with 0.15" bins. The red region represents 3-sigma uncertainties.

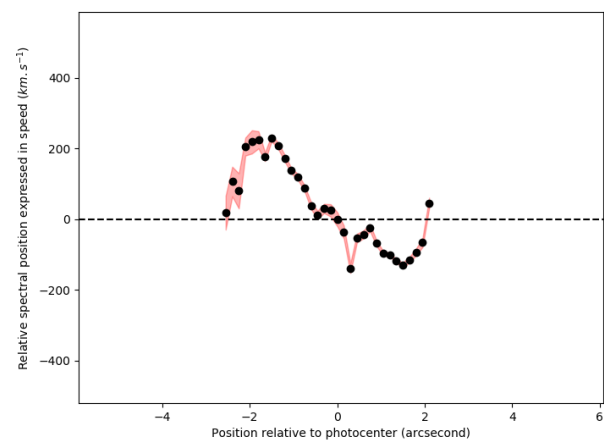


Fig. 13. Doppler shift of He I, measured from 0.15" bins. The speed is positive for a redshift and is measured relative to its value at the photocenter. The red region represents 3-sigma uncertainties.

width of the most prominent line (respectively 1118 nm and 1620 nm) in Figs. 15 and 16.

The equivalent width of 1118 nm exhibits a constant increase from North to South while the equivalent width of 1620 nm is at its minimum in the central region and increases in both direction while moving away from the the CE location. Due to the low SNR of 1590 nm and 1620 nm, and the overlapping of 1111 nm and 1118 nm, no doppler shift can be measured on those features.

4. Discussion

A young stellar cluster at the heart of NGC 1068?

Our results confirm the significant contribution of stellar light at the center of NGC 1068: except in the very central region where it accounts for $\sim 40\%$ of the flux, the stellar light largely dominates the spectrum in all the three bands of our observation (YJH). This large contribution is in good agreement with previous works such as Origlia et al. (1993), that concluded from absorption features that stellar light accounts for $\sim 70\%$ of the flux in the H-band in the $4.4'' \times 4.4''$ central region, or more

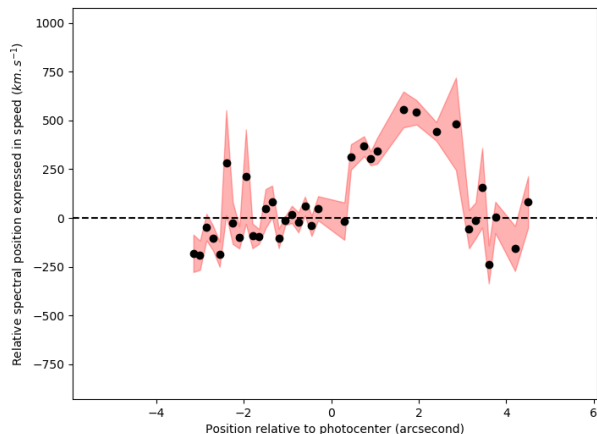


Fig. 14. Doppler shift of [FeII] 1643, measured from 0.15" bins. The speed is positive for a redshift and is measured relative to its value at the photocenter. The red region represents 3-sigma uncertainties.

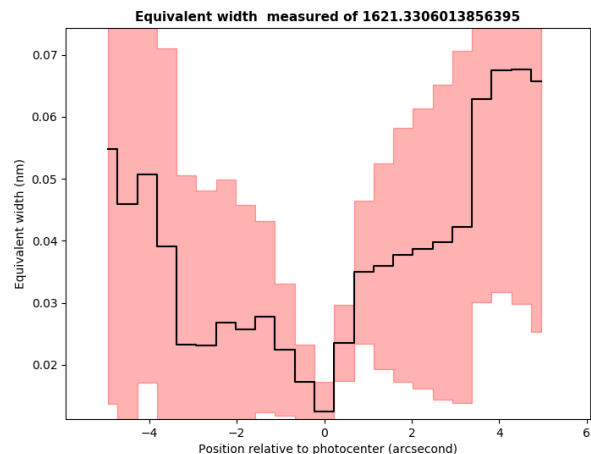


Fig. 16. Equivalent width of the 1620 nm absorption feature as function of the position along the slit, measured with 0.45" bins. The red region represents 3-sigma uncertainties.

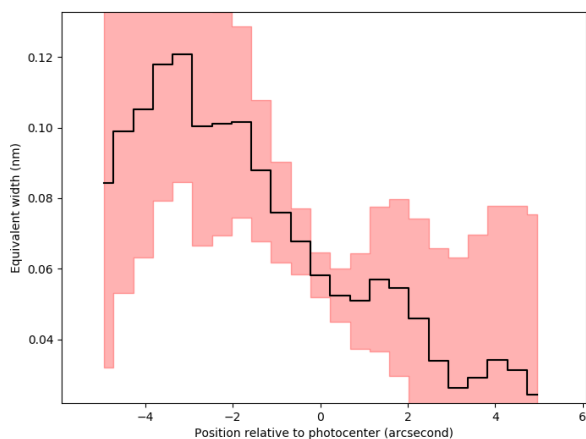


Fig. 15. Equivalent width of the 1118 nm absorption feature as function of the position along the slit, measured with 0.45" bins. Red region represents 3-sigma uncertainties

recently Storchi-Bergmann et al. (2012), that concluded from spectral synthesis in H and K bands that the stellar population dominates the spectrum in the inner 180 pc - 2".

Our analysis provided a well defined spatial profile for the stellar component (Fig. 8), revealing a central cluster with a 2" radial extent (whose center is collocated with the maximum of the 800 K emission) overimposed to the very young stellar background.

We have also been able to compare the observed continuum of this cluster to synthetic spectra of single stellar population (SSP) at different ages and found that a SSP of 120 Myr is able to describe it accurately, suggesting a recent starburst phase in this region. Davies et al. (2007a) also found clues of a starburst phase but quite older (250 Myr), which is in agreement with Martins et al. (2010b) whose stellar population synthesis indicates an intermediate age population together with some small contribution of young stars. Finally, Storchi-Bergmann et al. (2012) found the presence of two populations; one of 30 Myr, and the other one of 300 Myr, similar to Davies et al.

(2007a). Our age estimation for the central cluster then seems to be lower than those of the cited studies. However, considering that our method is mainly sensitive to the temperature of the stars, a slight excess of hot stars will easily be interpreted as more recent star formation when modeling the population with a SSP. We consider this as the best justification for the observed discrepancy but do not conclude on the origin of those hot stars, that could either be physically present in the central cluster or be a residual from the background subtraction. Beside this difference in the age estimation, the picture presented in this paper of a young stellar cluster surrounding the CE overimposed to a background composed of very hot stars is consistent with previous observations.

The last indicators of stellar population available in our data are the absorption features at 1111, 1118, 1590 and 1620 nm. Indeed the 1590 nm feature is mostly caused by Si I and the 1620 nm one is a CO bandhead. Both are tracing cold stars (G, K and early-M stars) as explained in Origlia et al. (1993). We find no variation in the ratio of these two lines along the slit and conclude that they trace a population with a uniform composition. The equivalent width of these features (Fig. 16) is consistent with the scheme already deduced from our continuum analysis : an extended stellar population diluted with other components in the central region. On the other hand, as suggested by Riffel et al. (2006) and Maraston (2005), the 1111 and 1118 nm features can be associated to CN absorption from ~1 Gyr thermal-pulsing AGB stars. However, the equivalent width along the slit of these features (Fig. 15) is quite different from the other stellar lines. It exhibits an almost constant increase from North to South without the expected dilution by the nucleus in the central region, clearly indicating that these lines originate from a structure different than the one probed with the Si I and CO absorption features. They could possibly trace an older stellar population, maybe the one detected by Davies et al. (2007a). The lack of dilution in the central region could also suggest that these lines arise from foreground interstellar material. However, we found no trace of interstellar absorption lines at these wavelength in dedicated catalogs, supporting the hypothesis of a stellar origin even if the spatial variation of the equivalent width remains unexplained.

Dust

The observed 800 K blackbody component is very likely tracing the obscuring dusty structure predicted by the unified model. The temperature is consistent with previous observations at longer wavelengths (Gratadour et al. 2003; Exposito et al. 2011; Storchi-Bergmann et al. 2012). This component's emission comes from an unresolved region ($< 0.4''$) at the location of the photocenter for which it is responsible for more than 50 % of the flux. No trace from the nodules observed at longer wavelength (Gratadour et al. 2005; Exposito et al. 2011) have been detected in our observation, probably due to our lower spatial resolution.

Spectroscopic observations of Seyfert 2 galaxies often exhibit a minimum in the near-infrared continuum emission, whose location varies from 1.1 to 1.4 μm (Riffel et al. 2006). In our analysis, we conclude that the position of this minimum is determined by the relative significance of stellar and dust components.

Contribution of scattered light to the continuum emission

Several studies pointed out that scattered-light from the central engine may significantly contribute to the near-infrared continuum: Crenshaw & Kraemer (2000) concluded that more than 69 % of the UV to NIR flux from the central region comes from the hidden nucleus, while Martins et al. (2010b) found a 25 % contribution to the 0.8 – 2.4 μm continuum in the center with peaks at 100-150 pc in both North and South directions. The latter observations are consistent with the presence of scattered light detected with polarimetric imaging both in the nuclear and circumnuclear regions by Gratadour et al. (2015). To measure the possible contribution of a Seyfert 1 nucleus to our spectrum we introduced a component with a flat spectrum in our model. Such a flat spectrum was observed in Seyfert 1 by Riffel et al. (2006). A significant contribution was clearly detected in the unresolved central region where hot dust is prevailing as well as a significant contribution from 2" to 4" South of the CE. This is very well explained by looking polarized intensity maps from Gratadour et al. (2015). A slit centered on the CE and orientated with $PA = 12^\circ$ intercepts two polarized regions: the first one in the very center, and the second one 3" South. The consistency between those results confirms the interpretation of polarized light as scattered light from the CE and our ability to detect it with λ^0 power-law. Note that the slope of the input scattered light (from $\lambda^{-1.5}$ as suggested by Crenshaw & Kraemer 2000, to λ^0 as presented in this paper) has very little impact on our results, since it is anyway very different from both the stellar and the hot dust components slopes (respectively $\sim \lambda^{-3}$ and $\sim \lambda^5$). It is then always detected at the same location with a similar contribution to the flux.

Ionised gas

Apart from [Fe II] lines, all the emission features detected in our observation follow a similar behavior, both in their spatial distribution and their doppler shift. We found that their position of maximum emission is located very near the photocenter, from exact colocation (He I, [P II], [S IX], Pa β) to 0.3" North ([S II]). The spatial extent of these emission lines goes up to 4" (limit of detection), with FWHM $\sim 1''$, and presents an asymmetry with a significant emission excess in the northern side of the slit.

This asymmetric behavior can be first explained by orientation effects. Indeed Das et al. (2006) concluded that the NLR is inclined toward us ($i = 5^\circ$), with its northern part being slightly closer to us than the southern one, and this orientation may favor the detection in the North of some regions whose southern counterparts are hidden from us. Secondly this emission line excess could alternatively arise from the nodules that have been detected in Gratadour et al. (2006) and already associated to emission lines in the K-band in Exposito et al. (2011). Higher angular resolution observation are needed to disentangle the role of those two possible causes in the asymmetric distribution of emission lines.

Supporting the first scenario, a significant Doppler shift is detected for these lines depending on the position on the slit, most probably tracing a radial outflow as observed in previous studies (Cecil et al. 2002; Das et al. 2006). We can observe with He I, the line with the clearest signal, a speed constantly increasing up to 1.5" (120 pc) followed by a quick drop back to rest speed at 2" (160 pc). The drop in speed seems to correlate very well with a structure detected both NIR polarimetric images (Gratadour et al. 2015). The spatial coincidence between the deceleration of the ionised gas and the scattering material indicates that the deceleration is probably caused by the interaction of the NLR with this structure.

Among the emission lines, the coronal lines (lines with ionization energy > 100 eV, [S IX] and [Si X] in our sample) seem to exhibit a narrower spatial profile. This observation is consistent with the scheme of photoionization from the strong nuclear UV-X continuum, whose intensity quickly decreases with the distance to the nucleus.

In comparison, the [Fe II] 1643 emission line reveals atypical features. First, it is detected in a much more extended region (i.e. twice the size of the emitting region of other lines). In the scenario involving photoionization by the central engine, this can be explained by its low ionization potential that allows ionization at greater distances from the source. However, it also appears that this emission line has a peak emission that does not coincide with the photocenter as other other lines do. This probably indicates a different structure, and possibly a different ionization mechanism. In order to test the possibility of shock induced ionization, we studied the [Fe II] 1643 / [P II] ratio, which is supposed to be sensitive to the ionization mechanism: values close to 1 indicate photoionization, while higher values (~ 10) indicate shocks. This diagnostic tool comes from the fact that iron is supposed to be locked in dust grain and that a strong [Fe II] emission indicates that dust grains must have been destroyed, shocks being the most plausible explanation. A similar diagnosis is performed in Oliva et al. (2001) and Hashimoto et al. (2011), with the [Fe II] 1257 line instead. The latter has the advantage of being close to [P II] and the diagnosis is then less sensitive to extinction. However in our case the measure of [Fe II] 1257 is too inaccurate due to its proximity with [S IX] and we prefer to use [Fe II] 1643 whose ratio with [Fe II] 1257 is fixed at 1.35 in the classical case B scenario from Osterbrock (1989). As shown in Fig. 17, this ratio stays well below 10 everywhere it can be measured, indicating that shocks do not play a significant role in the ionization of [Fe II] 1643.

Apart from its spatial distribution, the [Fe II] 1643 emission line also presents a very different velocity profile. Indeed, a Doppler redshift much more important than the one from the outflow ($v \sim 600 \text{ km.s}^{-1}$ vs $v \sim 200 \text{ km.s}^{-1}$) is affecting the line in the northern region. This difference confirms the previous suggestion that this emission arises from a different structure from

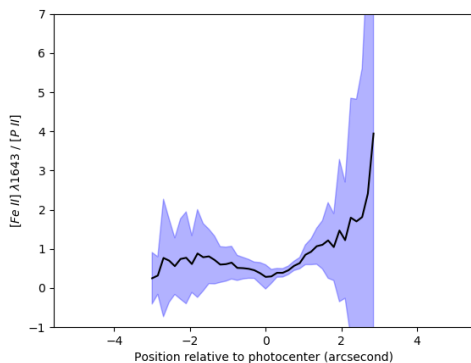


Fig. 17. Spatial distribution of the [Fe II] 1643 / [P II] ratio

the other emission lines, possibly tracing a foreground cloud of gas falling onto the central engine.

5. Conclusion

In order to understand the physical processes taking place in the central region of NGC 1068 we performed a long-slit spectroscopy analysis of the nucleus in YJH bands ($0.95 - 1.65 \mu\text{m}$) at sub-arcsecond angular resolution ($0.35''$).

We show that the continuum emission can be decomposed into four components: a young stellar population (120 Myr), hot dust (800 K), scattered light from the hidden Seyfert 1 nucleus and a very hot stellar background. In the very central region hot dust is the main contributor to the flux (more than 50 %) but scattered light is also significantly detected ($\sim 10\%$). Elsewhere the stellar content dominates the continuum emission, with an extended very hot stellar population covering all the slit and a cuspy 120 Myr stellar population around the photocenter.

Absorption features at 1.59 and $1.62 \mu\text{m}$ tracing cold stars are detected in an extended region, supporting the previous conclusion that stellar content is the main contributor to the observed flux.

Many emission lines are detected, tracing the Narrow Line Region of NGC 1068. Almost all those emission lines have their maximum emission in the central $0.5''$, supporting the hypothesis of photoionization from the central engine. Moreover, our analysis of the [Fe II] 1643 / [P II] does not support a shock induced ionization scenario. A Doppler shift has been measured in several of those lines ([S II], He I, [P II], Pa β), leading to the conclusion that they are tracing the outflow originating from around the nucleus whose northern part is moving toward the observer and southern part away from it.

The [Fe II] emission lines' features are quite different. Their spatial distribution is more extended, their position of maximum emission is offset North to the nucleus, and they present a very different Doppler shift. We conclude that they arise from a distinct structure, possibly tracing an inflow to central engine.

This study revealed the potential of the YJH bands for the study of Seyfert 2 nuclei. We think that full AO correction could bring valuable additional information, in particular for the study of the very central region. Moreover, other slit orientations could probe locations of interest, in particular the small nodules surrounding the nucleus and the polarized spots detected in the circumnuclear region.

References

- Antonucci, R. 1993, *ARA&A*, 31, 473
- Antonucci, R. R. J. & Miller, J. S. 1985, *ApJ*, 297, 621
- Beuzit, J.-L., Feldt, M., Dohlen, K., et al. 2008, in *Proc. SPIE*, Vol. 7014, Ground-based and Airborne Instrumentation for Astronomy II, 701418
- Bock, J. J., Neugebauer, G., Matthews, K., et al. 2000, *AJ*, 120, 2904
- Cecil, G., Dopita, M. A., Groves, B., et al. 2002, *ApJ*, 568, 627
- Crenshaw, D. M. & Kraemer, S. B. 2000, *ApJ*, 532, 247
- Cutri, R. M., Skrutskie, M. F., van Dyk, S., et al. 2003, *VizieR Online Data Catalog*, II/246
- Das, V., Crenshaw, D. M., Kraemer, S. B., & Deo, R. P. 2006, *AJ*, 132, 620
- Davies, R., Genzel, R., Tacconi, L., Müller Sánchez, F., & Sternberg, A. 2007a, in *The Central Engine of Active Galactic Nuclei*, Vol. 373, 639
- Davies, R. I., Müller Sánchez, F., Genzel, R., et al. 2007b, *ApJ*, 671, 1388
- Dopita, M. A. & Sutherland, R. S. 1996, *ApJS*, 102, 161
- Exposito, J., Gratadour, D., Clénet, Y., & Rouan, D. 2011, *A&A*, 533, A63
- Gallimore, J. F., Baum, S. A., O'Dea, C. P., & Pedlar, A. 1996, *ApJ*, 458, 136
- Gratadour, D., Clénet, Y., Rouan, D., Lai, O., & Forveille, T. 2003, *A&A*, 411, 335
- Gratadour, D., Rouan, D., Grosset, L., Boccaletti, A., & Clénet, Y. 2015, *A&A*, 581, L8
- Gratadour, D., Rouan, D., Mugnier, L. M., et al. 2006, *A&A*, 446, 813
- Gratadour, D., Rouan, D., Boccaletti, A., Riaud, P., & Clénet, Y. 2005, *A&A*, 429, 433
- Hashimoto, T., Nagao, T., Yanagisawa, K., Matsuoka, K., & Araki, N. 2011, *Publications of the Astronomical Society of Japan*, 63, L7
- Hickox, R. C. & Alexander, D. M. 2018, *ARA&A*, 56, 625
- Jaffe, W., Meisenheimer, K., Röttgering, H. J. A., et al. 2004, *Nature*, 429, 47
- Kormendy, J., Bender, R., & Cornell, M. E. 2011, *Nature*, 469, 374
- Kotulla, R., Fritze, U., Weilbacher, P., & Anders, P. 2009, *MNRAS*, 396, 462
- Kraemer, S. B. & Crenshaw, D. M. 2000, *ApJ*, 544, 763
- Macchetto, F., Capetti, A., Sparks, W. B., Axon, D. J., & Boksenberg, A. 1994, *ApJ*, 435, L15
- Maraston, C. 2005, *MNRAS*, 362, 799
- Martins, L. P., Riffel, R., Rodríguez-Ardila, A., Gruenwald, R., & de Souza, R. 2010a, *MNRAS*, 406, 2185
- Martins, L. P., Rodríguez-Ardila, A., de Souza, R., & Gruenwald, R. 2010b, *MNRAS*, 406, 2168
- Mor, R. & Netzer, H. 2012, *Monthly Notices of the Royal Astronomical Society*, 420, 526
- Nazarova, L. 1996, *Vistas in Astronomy*, 40, 35, proceedings of the Oxford Torus Workshop
- Oliva, E., Marconi, A., Maiolino, R., et al. 2001, *A&A*, 369, L5
- Origlia, L., Moorwood, A. F. M., & Oliva, E. 1993, *A&A*, 280, 536
- Osterbrock, D. E. 1989, *Astrophysics of gaseous nebulae and active galactic nuclei*
- Pickles, A. J. 1998, *PASP*, 110, 863
- Pier, E. A., Antonucci, R., Hurt, T., Kriss, G., & Krolik, J. 1994, *ApJ*, 428, 124
- Poncellet, A., Perrin, G., & Sol, H. 2006, *A&A*, 450, 483
- Rees, M. J. 1984, *ARA&A*, 22, 471
- Riffel, R., Rodríguez-Ardila, A., & Pastoriza, M. G. 2006, *A&A*, 457, 61
- Riffel, R. A., Vale, T. B., Storchi-Bergmann, T., & McGregor, P. J. 2014, *MNRAS*, 442, 656
- Romeo, A. B. & Fathi, K. 2016, *MNRAS*, 460, 2360
- Storchi-Bergmann, T., Riffel, R. A., Riffel, R., et al. 2012, *ApJ*, 755, 87
- Vigan, A., Langlois, M., Moutou, C., & Dohlen, K. 2008, *A&A*, 489, 1345
- Wilson, A. S. & Ulvestad, J. S. 1983, *ApJ*, 275, 8

Appendix A: Lines profiles

Fig. A.1. Profile of absorption feature at 1111 nm

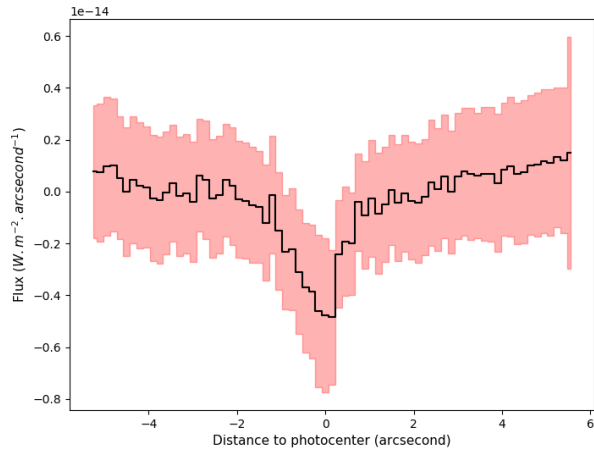
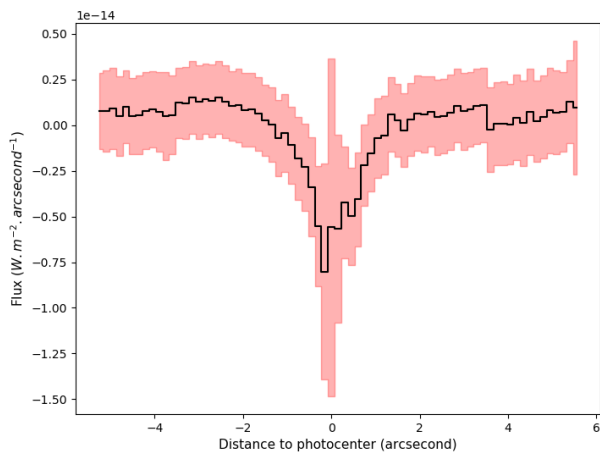


Fig. A.2. Profile of absorption feature at 1590 nm



Appendix B: Emission lines doppler shift

Fig. A.3. Profile of He II

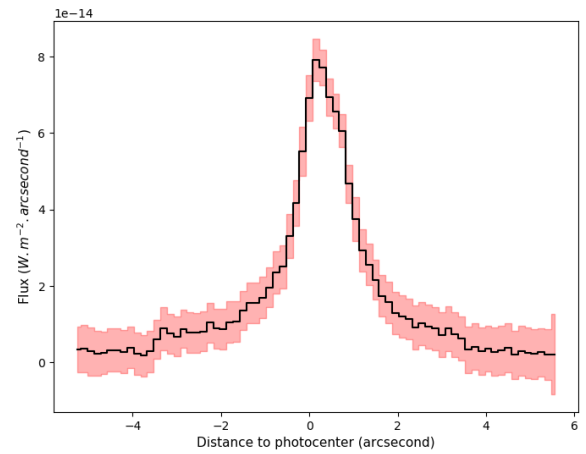


Fig. A.4. Profile of [S II]

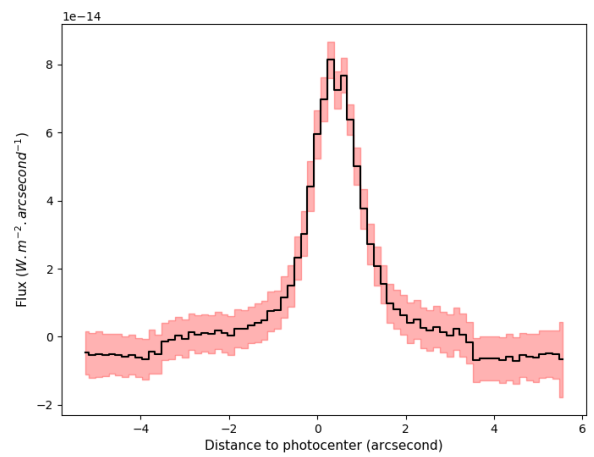


Fig. A.5. Profile of Paschen Gamma

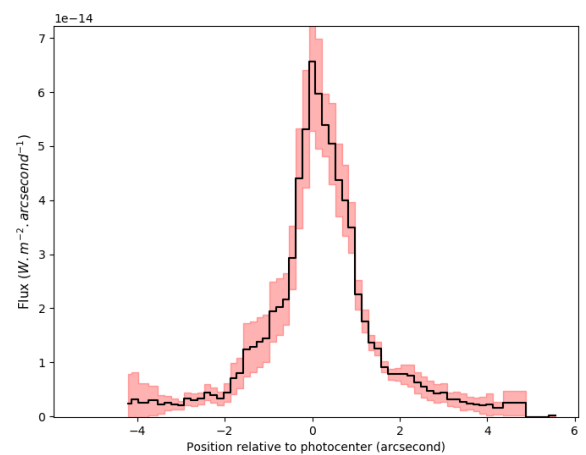


Fig. A.6. Profile of [P II]

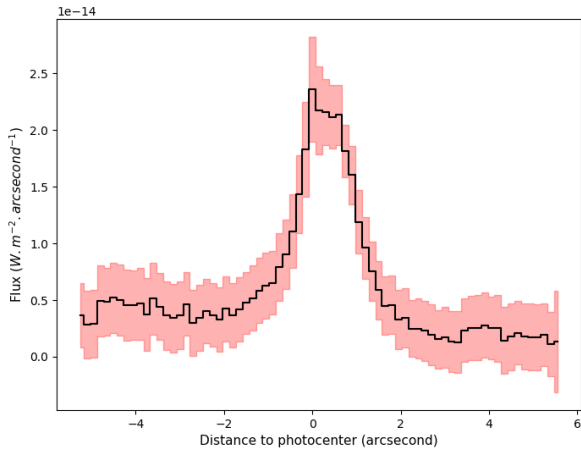


Fig. A.9. Profile of Paschen Beta

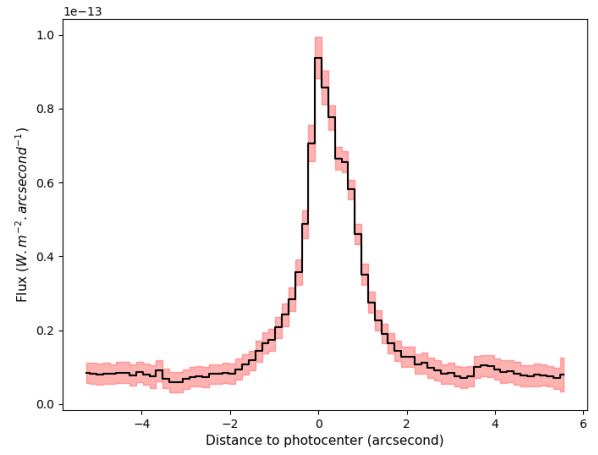


Fig. A.7. Profile of [S IX]

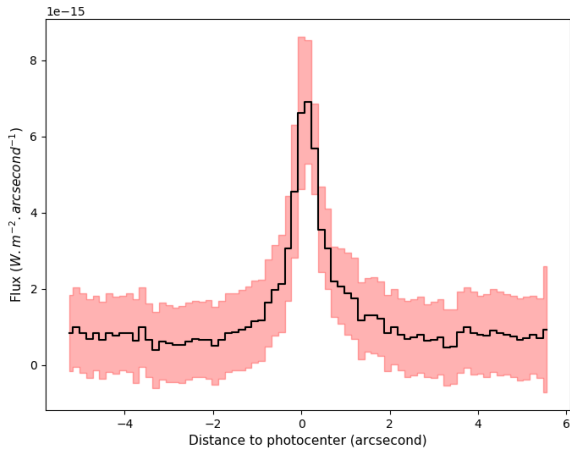


Fig. A.10. Profile of [Si X]

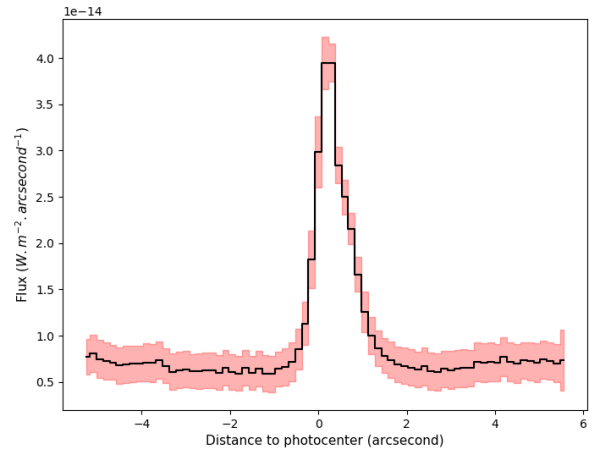


Fig. A.8. Profile of [Fe II] 1257

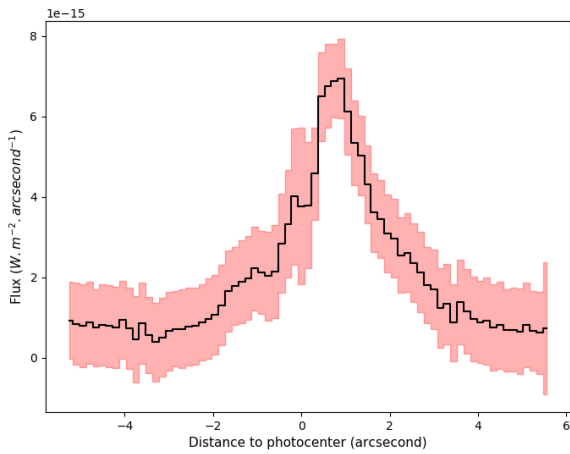


Fig. B.1. Doppler shift of [S II]

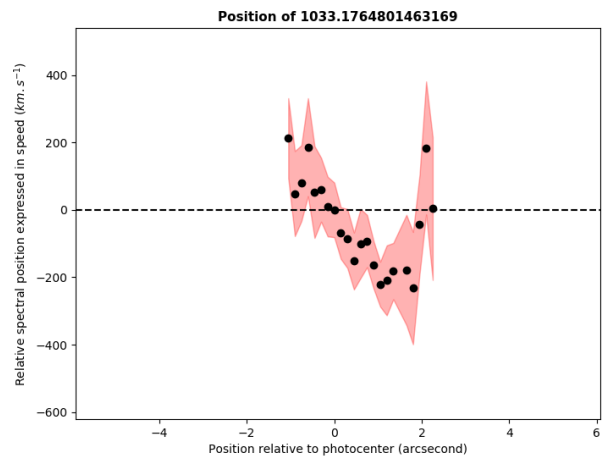
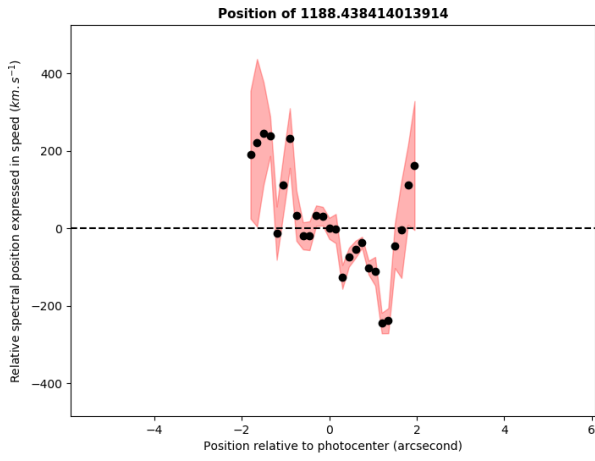


Fig. B.2. Doppler shift of [P II]**Fig. B.3.** Doppler shift of Paschen Beta